High-resolution 3DFT MR imaging of the endolymphatic duct and soft tissues of the otic capsule.

M Brogan, D W Chakeres and P Schmalbrock

AJNR Am J Neuroradiol 1991, 12 (1) 1-11
http://www.ajnr.org/content/12/1/1

High-Resolution 3DFT MR Imaging of the Endolymphatic Duct and Soft Tissues of the Otic Capsule

Martha Brogan[1]
Donald W. Chakeres
Petra Schmalbrock

This study compares the visualization of otic capsule anatomy by thin-section three-dimensional Fourier transformation (3DFT) MR imaging with that by high-resolution CT. The osseous margins of the otic capsule are delineated by high-resolution CT, while MR displays the soft-tissue structures. Routine two-dimensional Fourier transformation (2DFT) spin-echo MR techniques have been limited by slice thickness and signal to noise. Previous longer TE 3DFT gradient-echo MR images of the otic structures have been degraded by magnetic susceptibility effects, which limit spatial resolution and decrease signal to noise. These effects are especially prevalent in the otic capsule, where small soft-tissue structures interface with surrounding air and bone. We developed a high-resolution 3DFT MR technique to image five normal subjects. MR images were compared with high-resolution CT images of the same subjects. Axial, sagittal, and coronal 3DFT gradient-echo MR images with a short TR/TE and 15° flip angle were acquired on a General Electric 1.5-T Signa unit using a 3-in. circular, receive-only surface coil. Axial, sagittal, and coronal 1.5-mm-thick contiguous high-resolution CT bone-algorithm images were obtained also. There was a high correlation between the MR and CT findings. The 3DFT MR images demonstrated significantly higher spatial resolution and soft-tissue detail than the high-resolution CT images did. For example, the endolymphatic duct was seen on twice the number of consecutive sagittal and axial MR slices. Other soft-tissue otic capsule structures routinely seen on the 3DFT MR images included the entire facial nerve, membranous labyrinth including cochlea, and tensor tympani muscle.

This study demonstrates a new high-resolution 3DFT MR technique for visualizing the soft-tissue microstructures of the otic capsule and achieves a level of spatial resolution beyond that possible with high-resolution CT.

***AJNR* 12:1–11, January/February 1991**

The soft-tissue structures of the otic capsule are embedded in a dense bony matrix. MR imaging has been found to be the best technique for imaging soft-tissue abnormalities of the brain [1–6]. High-resolution CT is best for demonstrating small bony and air-space changes of the temporal bone [1, 7]. Therefore, both high-resolution CT and MR techniques play an important role in diagnostic imaging of the otic capsule. In combination, these techniques provide fine bony detail (high-resolution CT), high soft-tissue contrast, and multiplanar high-resolution anatomic detail (MR), to provide the most complete diagnostic imaging of the otic capsule.

Current high-resolution CT imaging of the otic capsule uses a bone-algorithm technique that demonstrates excellent bony detail, but may not accurately reflect early pathologic changes in the soft-tissue components of the otic capsule. Partial-volume averaging of small soft-tissue and bony structures, beam-hardening effects, and slice thickness limitations (1.0 mm) contribute to limited spatial resolution [8]. Precise patient positioning requirements and ionizing radiation doses inherent in high-resolution CT are not features of MR.

Two-dimensional Fourier transformation (2DFT) spin-echo MR imaging techniques have improved and currently are the standard for evaluating cerebellopontine

Received April 26, 1990; revision requested July 12, 1990; revision received August 17, 1990; accepted September 3, 1990.

[1] All authors: Department of Radiology, Division of Neuroradiology, S-209 Rhodes Hall, 450 W. Tenth Ave., Columbus, OH 43210. Address reprint requests to M. Brogan.

0195-6108/91/1201-0001

angle (CPA) disease [2]. Early pathologic changes in the otic capsule seen on MR have been reported [9]. A limitation inherent in the standard 2DFT spin-echo technique is relatively thick slices (3 mm). This spatial resolution does not approach that of high-resolution CT and is inadequate for most of the small structures of the otic capsule. The short TR 2DFT spin-echo technique is relatively T1-weighted and not optimal for imaging fluid-filled structures of the otic capsule. Long TR/TE T2-weighted spin-echo MR techniques have limited signal to noise. Also, the long acquisition times contribute to image degradation related to increased patient motion and signal loss.

Recently, three-dimensional Fourier transformation (3DFT) gradient-echo MR imaging has become available with shorter acquisition times and higher resolution [10–13]. Application of this technique to imaging the otic capsule has been limited by the relatively long TEs (12–20 msec). The magnetic susceptibility effects of the interfaces between bone, air, and otic capsule soft-tissue structures have led to poor image quality [14]. In fact, loss of anatomic detail in areas adjacent to these interfaces has limited the use of this technique in primary imaging of the brain. We developed a 3DFT gradient-echo technique that employs a very short TE to overcome some of these limitations. We have applied this technique to imaging the soft-tissue structures of the otic capsule [12]. The millimeter-thick slices (high resolution), short TE (limited signal loss secondary to magnetic susceptibility effects), and low flip angle (limited T1-weighting) available in this 3DFT technique allow superb spatial resolution and signal to noise with clini-

Key to Abbreviations Used in Figures

a	ampulla
at	apical turn of cochlea
bt	basal turn of cochlea
c	cochlea
ca	cochlear aqueduct
cc	carotid canal
cpa	cerebellopontine angle
csa	canal of subarcuate artery
eac	external auditory canal
f	fundus
fn	facial nerve
fnc	facial nerve canal
gg	geniculate ganglion
iac	internal auditory canal
ica	internal carotid artery
jv	jugular vein
lsc	lateral semicircular canal
ow	oval window
pg	posterior genu of facial nerve
psc	posterior semicircular canal
rw	round window
ss	sigmoid sinus
ssc	superior semicircular canal
st	second turn of cochlea
ttm	tensor tympani muscle
v	vestibule
va	vestibular aqueduct

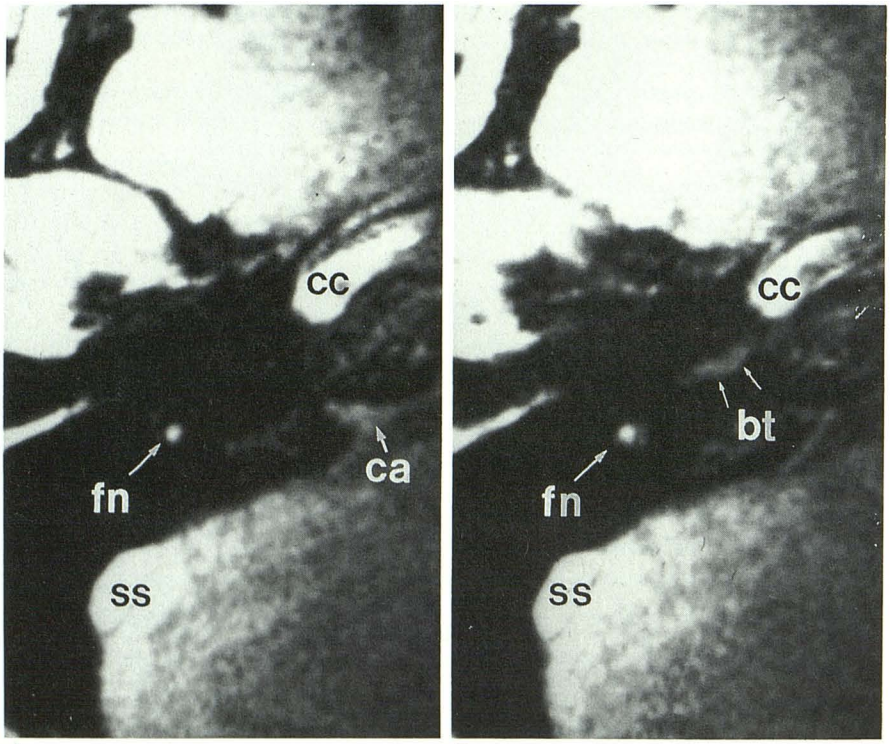

Fig. 1.—Axial 3DFT MR images, 33/7/1 (256 × 256 matrix and 1.0-mm slice thickness). See key for abbreviations.

***A*, At level of right cochlear aqueduct. Flared high-signal cochlear aqueduct (ca) is seen.**

***B*, 1.0 mm rostrad. High-signal endolymph and perilymph within basal turn (bt) of cochlea are seen.**

Flow-related high signal intensity is present within lumen of carotid canal (cc) and sigmoid sinus (ss).

cally feasible acquisition times. While this initial study demonstrates the application of 3DFT to temporal bone imaging, it is not intended to represent a detailed comparative study of 3DFT MR imaging techniques.

Subjects and Methods

The temporal bones of five normal volunteers 27–41 years old were imaged with high-resolution 3DFT MR and CT techniques (Figs. 1–15). The MR images were obtained on a General Electric 1.5-T

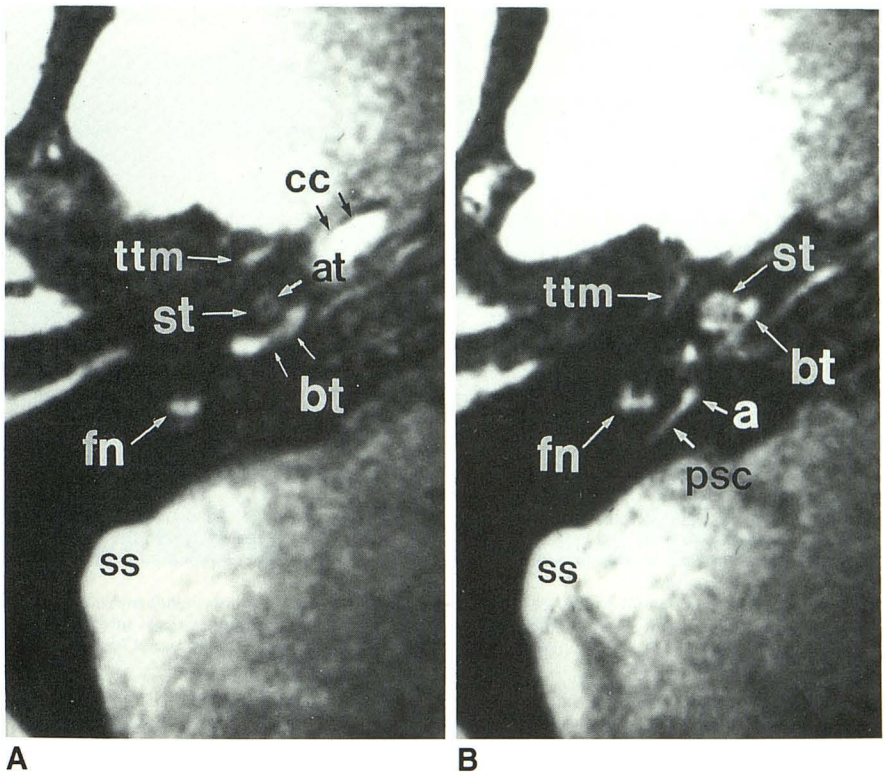

Fig. 2.—Axial 3DFT MR images. See key for abbreviations.

A, At level of right basal and second turns of cochlea. High-signal second (st) and basal (bt) turns of cochlea lie immediately posterior to carotid canal (cc). Linear high-signal tensor tympani muscle (ttm) is seen in signal void of anterior aspect of middle ear cavity.

B, 1.0 mm rostrad. High signal is seen from endolymph and perilymph within portions of cochlea and posterior semicircular canal (psc), including ampulla (a).

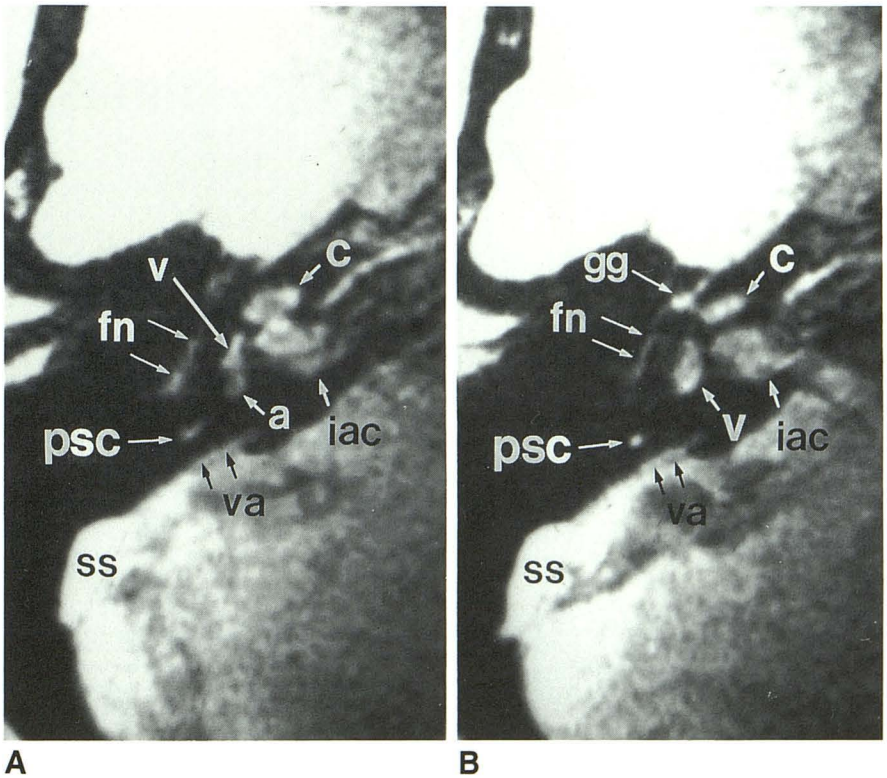

Fig. 3.—Axial 3DFT MR images. See key for abbreviations.

A, At level of right internal auditory canal. Endolymphatic sac within distal segment of vestibular aqueduct (va) is seen paralleling posterior semicircular canal (psc) within signal void of posterior aspect of petrous bone near sigmoid sinus (ss).

B, 1.0 mm rostrad. Geniculate ganglion (gg) lateral to cochlea (c) is seen.

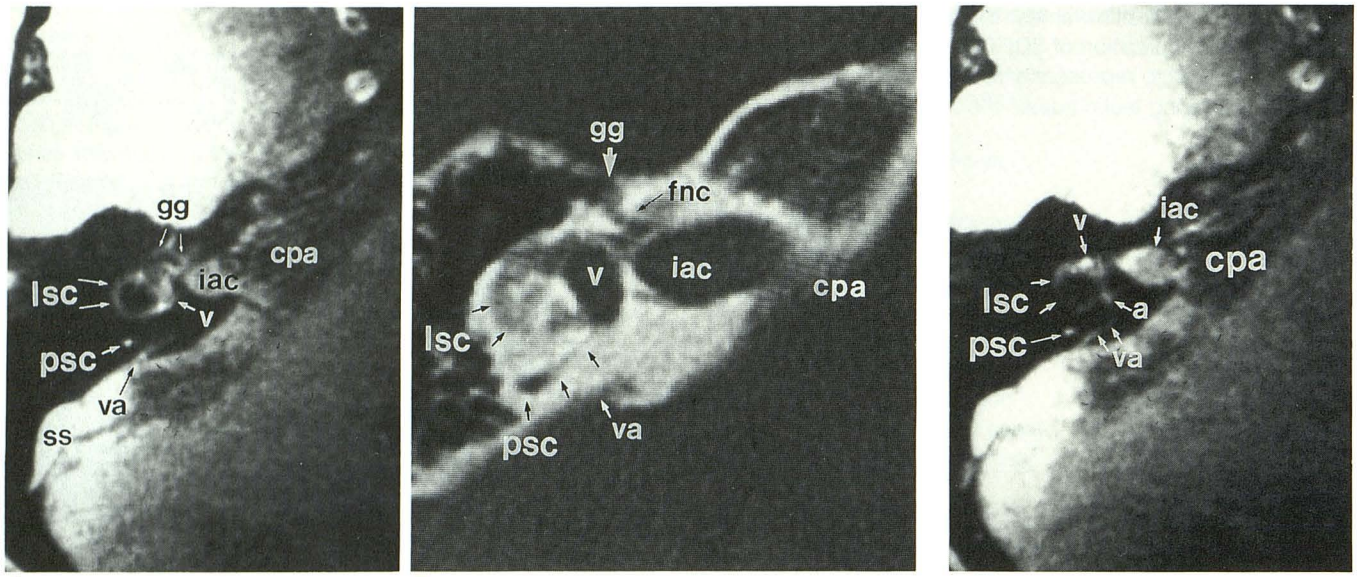

Fig. 4.—*A*, Axial 3DFT MR image at level of right lateral semicircular canal. Lateral semicircular canal (lsc) is seen as semicircular high-signal focus. Anteriorly, inverted V-shaped proximal and distal limbs of geniculate ganglion (gg) are seen. Posteriorly, endolymphatic duct and sac within vestibular aqueduct (va) course parallel to posterior semicircular canal (psc). Note higher signal from CSF within lumen of the internal auditory canal (iac) compared with that of adjacent cerebellopontine angle (cpa), a finding that suggests relative stasis.

B, Axial high-resolution CT image at level of right internal auditory canal. Facial nerve canal (fnc) is seen arising from fundus of IAC and coursing toward geniculate ganglion (gg). Inferior aspect of vestibular aqueduct (va) is seen posterior and parallel to posterior semicircular canal (psc).

See key for abbreviations.

Fig. 5.—Axial 3DFT MR image at level of right lateral semicircular canal. High-signal endolymph within endolymphatic duct is seen coursing posterior and parallel to posterior semicircular canal (psc) within vestibular aqueduct (va). See key for abbreviations.

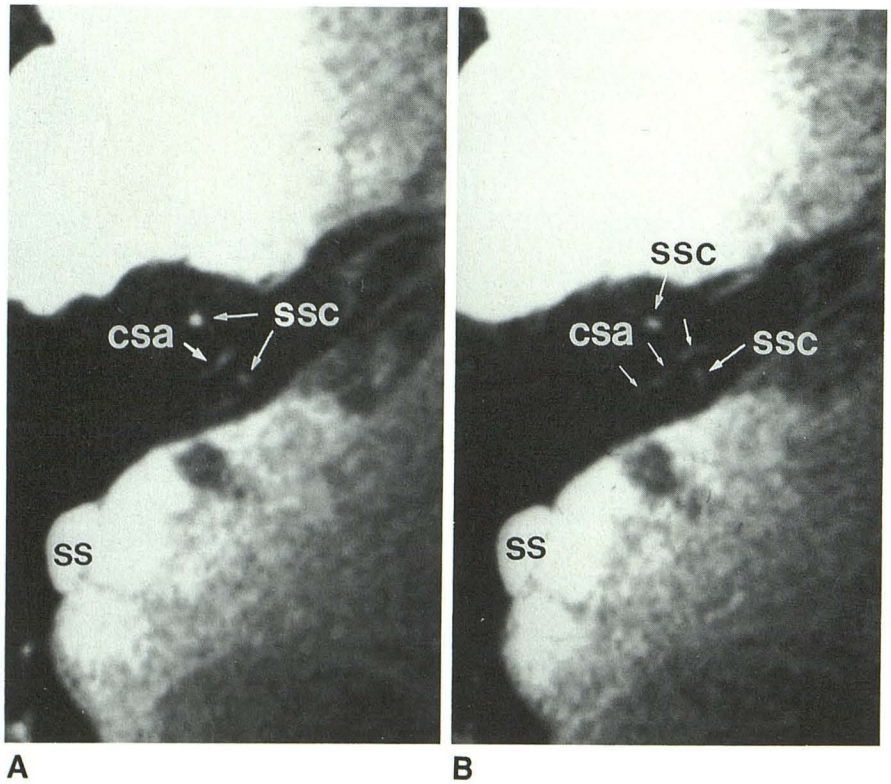

Fig. 6.—Axial 3DFT MR images. See key for abbreviations.

A, At level of right canal of subarcuate artery. Soft-tissue contents within canal of subarcuate artery (csa) appear as thin, linear, smoothly arching high signal intensity coursing deep into otic capsule between anterior and posterior limbs of superior semicircular canal (ssc).

B, 1.0 mm rostrad.

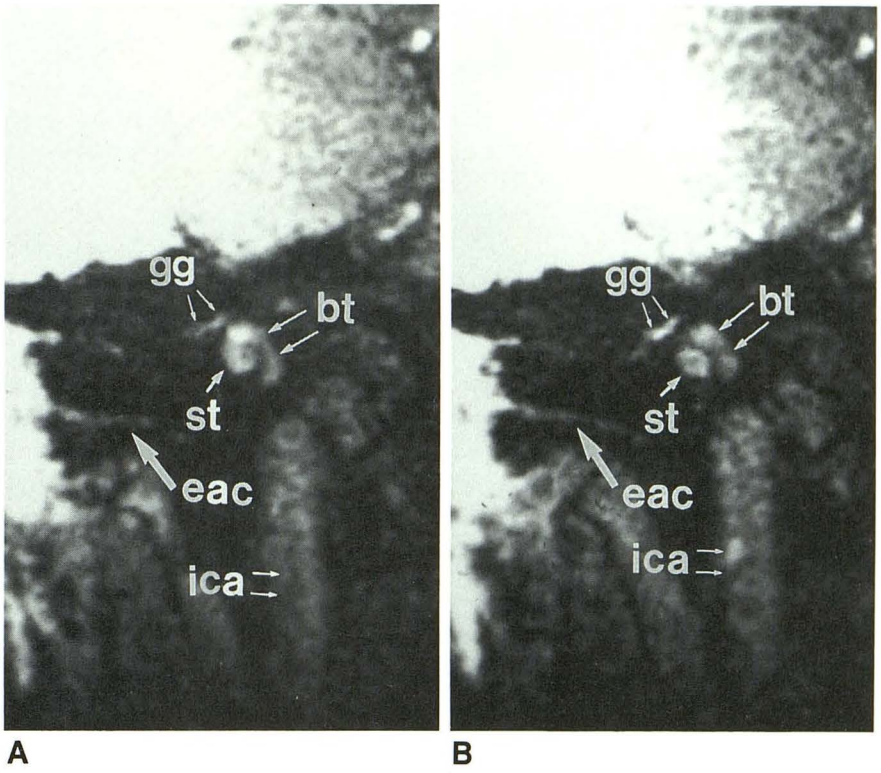

Fig. 7.—Coronal 3DFT MR images. See key for abbreviations.

***A*, At level of right cochlea. Second (st) and basal (bt) turns of cochlea are seen coiled in configuration of snail shell close to crescent-shaped geniculate ganglion (gg).**

***B*, 1.0 mm anteriad. High-signal periosteum lining floor of external auditory canal (eac) is seen. High flow-related signal delineates cervical portion of internal carotid artery (ica).**

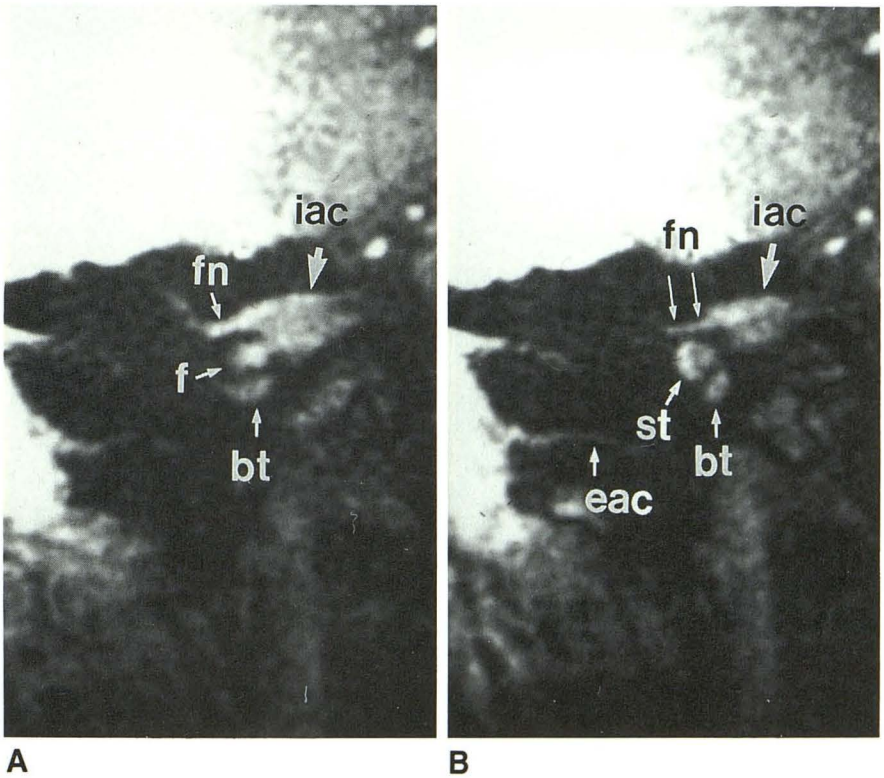

Fig. 8.—Coronal 3DFT MR images. See key for abbreviations.

***A*, At level of right internal auditory canal. Facial nerve (fn) is seen leaving fundus (f) of internal auditory canal to form proximal limb of geniculate ganglion (gg).**

***B*, 1.0 mm anteriad. Basal (bt) and second (st) turns of cochlea are also seen.**

Signa unit (Milwaukee, WI). The subjects were scanned with the neck in slight flexion to align the horizontal semicircular canal parallel to the axial scan plane. This is 30° above the anthropologic baseline [7]. Direct sagittal and 120° coronal MR images were obtained.

3DFT MR images were obtained by using a gradient-recalled acquisition in a steady state (GRASS) technique, 33/7/1 (TR/TE/excitation), 15° flip angle, 1.0-mm slice thickness, 12-cm field of view (FOV), and 256 × 256 matrix [15]. Acquisition time was 4.5 min. The

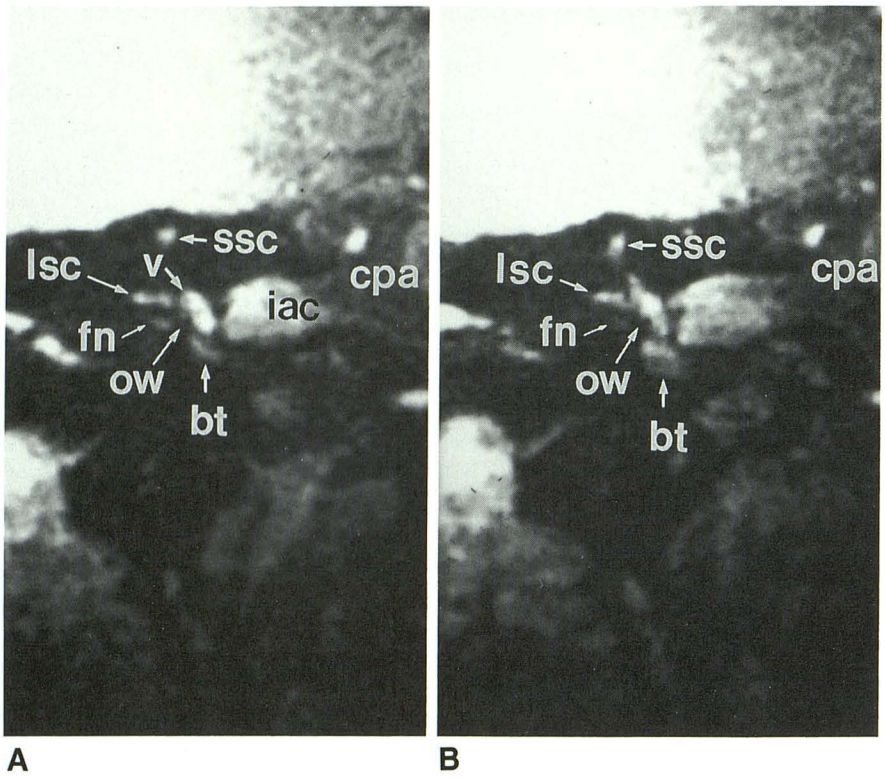

Fig. 9.—Coronal 3DFT MR images. See key for abbreviations.

A, At level of right vestibule. Horizontal facial nerve (fn) is seen coursing inferior to lateral semicircular canal (lsc). Oval window (ow) is not seen directly, but can be approximated by location of horizontal portion of facial nerve (fn) and cochlea. Note higher signal intensity of CSF in internal auditory canal than in the cerebellopontine angle.

B, 1.0 mm anteriad.

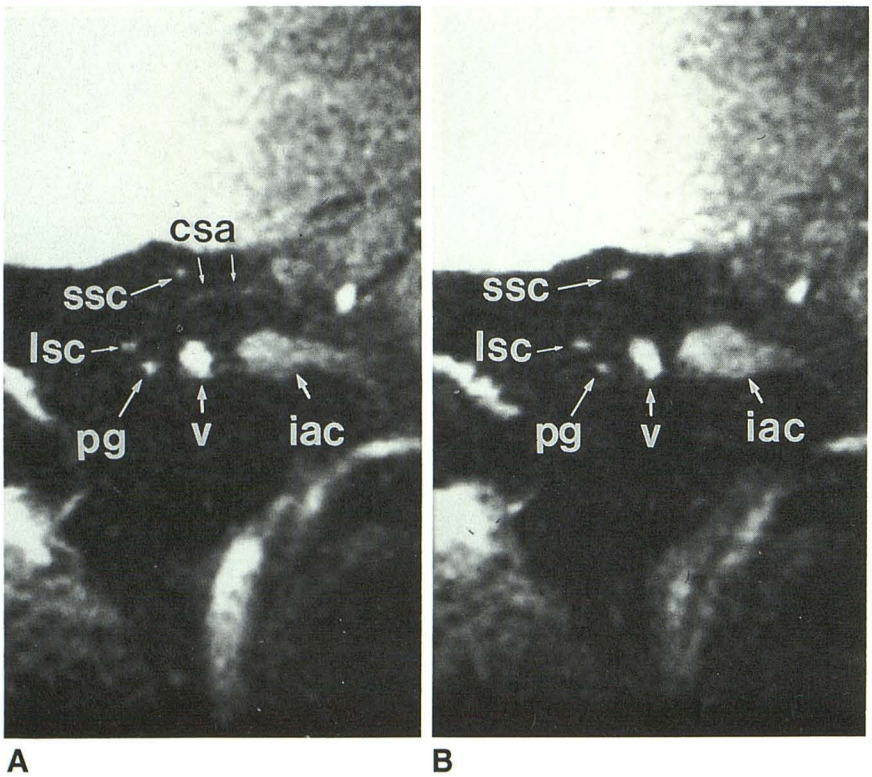

Fig. 10.—Coronal 3DFT MR images. See key for abbreviations.

A, At level of right vestibule. Contents of canal of subarcuate artery (csa) are seen coursing medially below superior semicircular canals (ssc). Posterior genu of facial nerve (pg) is seen inferior to lateral semicircular canal (lsc).

B, 1.0 mm anteriad.

shortest available TR (33 msec) was used to minimize image acquisition times. A short TE was chosen to minimize the loss of signal to noise inherent in longer TEs. The shortest achievable TE for high resolution without the use of flow-compensation gradients was 7 msec. The low flip angle of 15° was used to minimize the T1-weighting, which contributed to increased signal intensity from the fluid-filled structures of the otic capsule. Adequate signal to noise was achieved with a slice thickness of 1.0 mm. Thinner slices (0.5

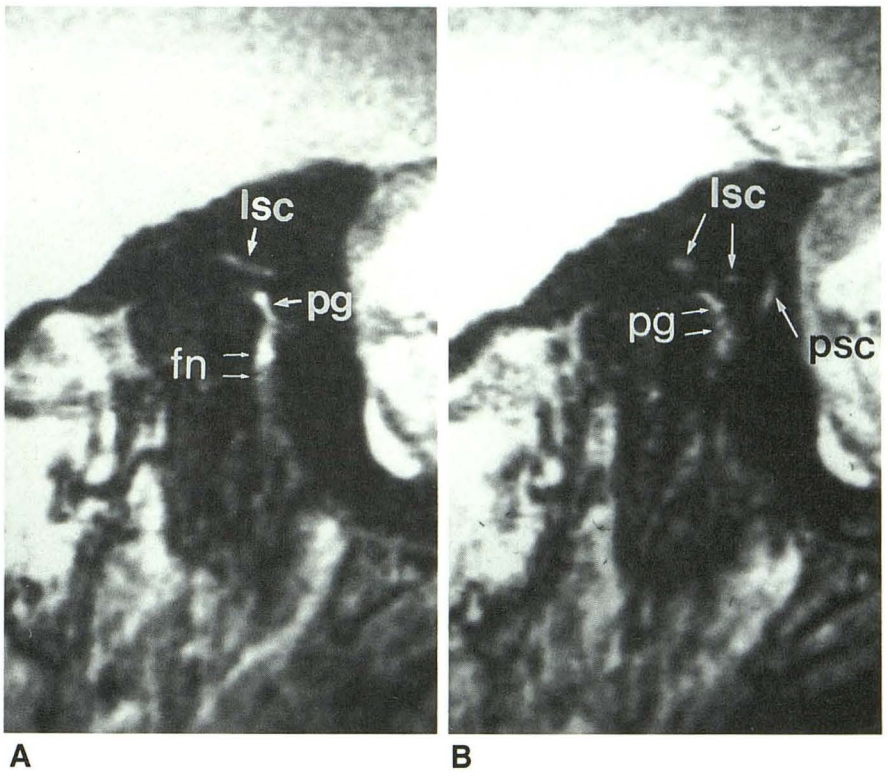

Fig. 11.—Sagittal 3DFT MR images. See key for abbreviations.

***A*, At level of posterior genu of right facial nerve. On the left, facial nerve (fn) is seen in region of posterior genu (pg). Apex of lateral semicircular canal (lsc) is also seen.**

***B*, 1.0 mm mediad. Portions of lateral (lsc) and posterior (psc) semicircular canals are seen.**

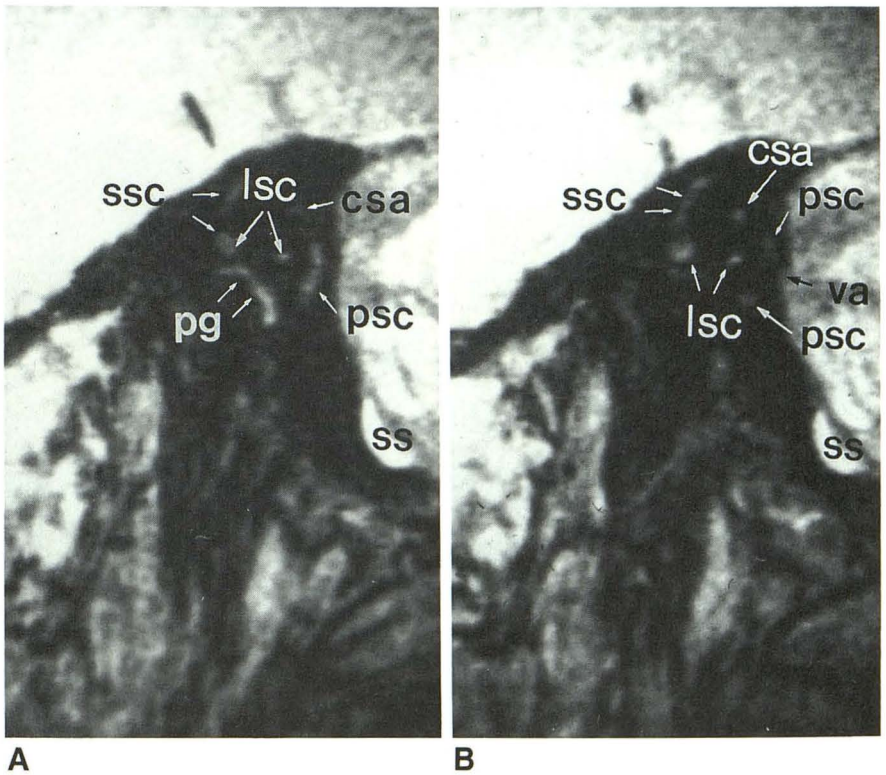

Fig. 12.—Sagittal 3DFT MR images. See key for abbreviations.

***A*, At level of right semicircular canals. Portions of superior, lateral, and posterior semicircular canals are seen in cross section.**

***B*, 1.0 mm mediad. Lateral portion of endolymphatic sac is seen within vestibular aqueduct. Contents of canal of subarcuate artery are seen inferior to superior semicircular canal.**

mm) were available, but the gain in spatial resolution was offset by a loss in signal to noise. Voxel dimensions with a 1.0-mm slice thickness in a 12-cm FOV were 0.47 × 0.47 × 1.0 mm.

The standard head coil was limited to a minimum FOV of 16 cm because of poor signal to noise. Images obtained using the head coil with a small FOV were also degraded by wraparound artifact. Off-center FOV was also needed for head coil examinations. Significantly improved image quality was obtained with a 3-in. receive-only surface

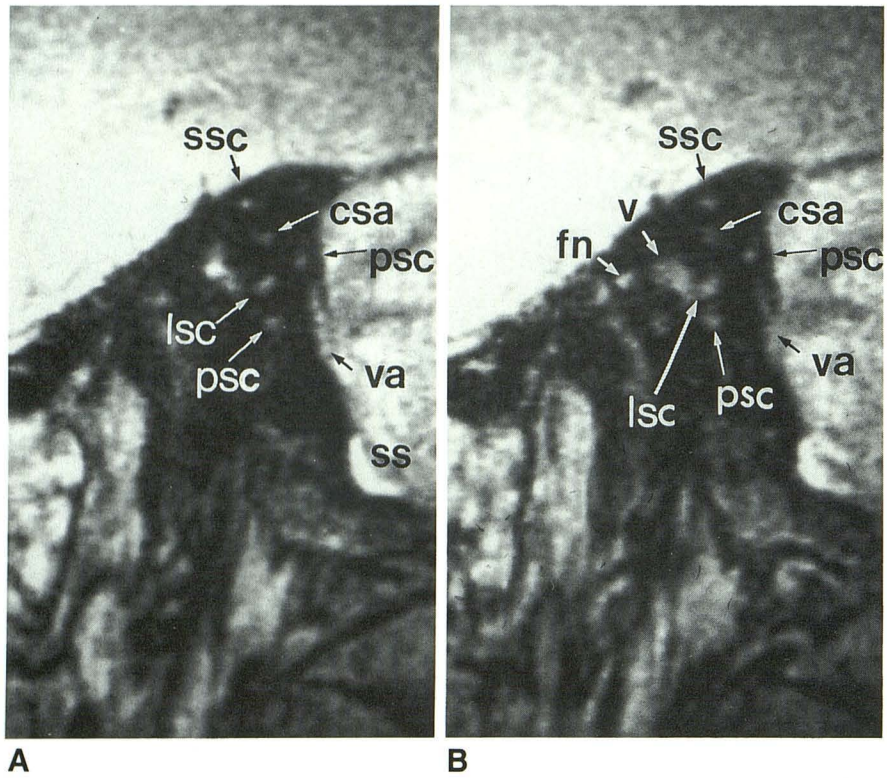

Fig. 13.—Sagittal 3DFT MR images. See key for abbreviations.

A, At level of right vestibule. Endolymphatic duct and sac are seen within vestibular aqueduct (va) along posterior aspect of petrous bone near sigmoid sinus (ss).

B, Image 1.0 mm mediad shows canal of subarcuate artery (csa).

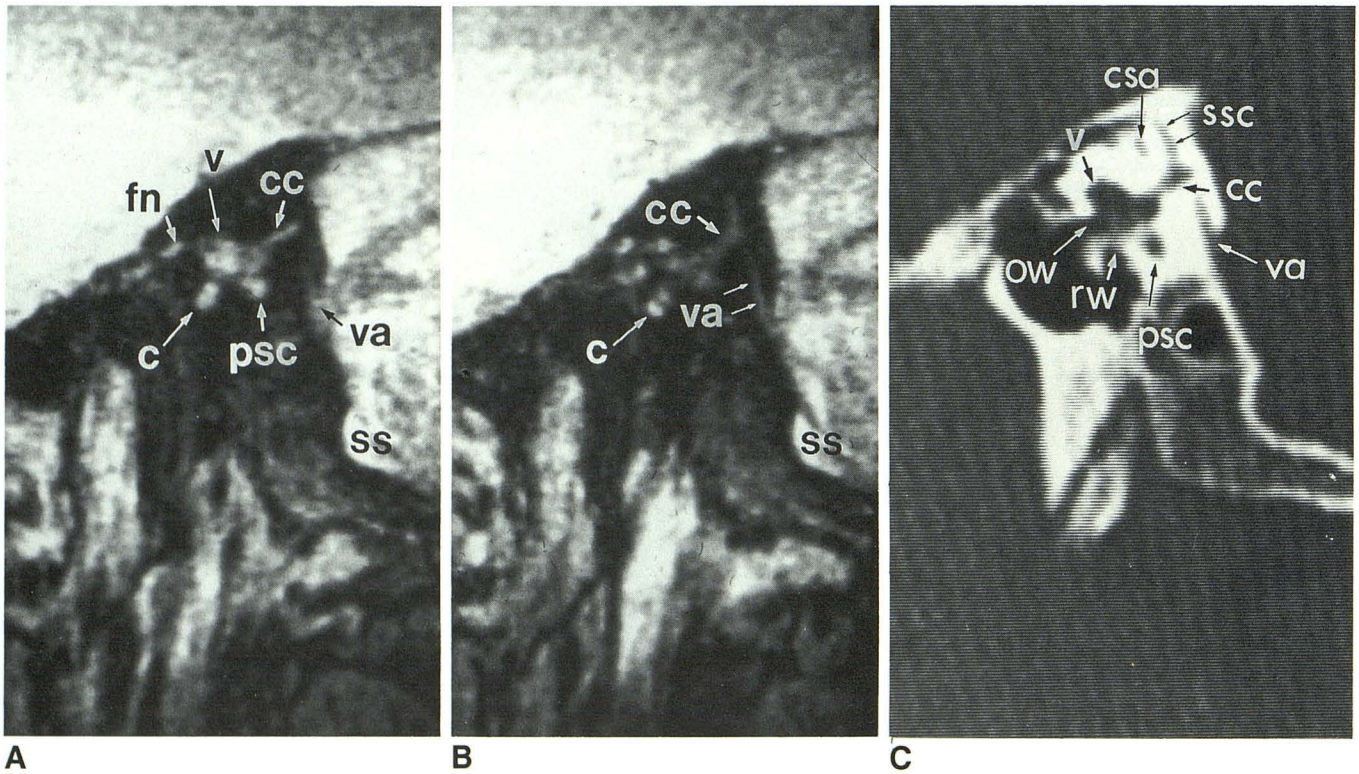

Fig. 14.—*A*, Sagittal 3DFT MR image at level of right vestibular aqueduct. Common crus (cc) arises from superior and posterior aspect of vestibule (v). Anterior to vestibule, a portion of facial nerve (fn) is seen in region of geniculate ganglion. Posteriorly, endolymphatic duct lies within vestibular aqueduct (va).

B, 1.0 mm mediad. Proximity of vestibular aqueduct (va) to common crus (cc) is seen.

C, Sagittal high-resolution CT image at level of right round window. Oval (ow) and round (rw) windows are seen on inferior aspect of vestibule (v). Vestibular aqueduct (va) courses along posterior petrous bone in proximity to common crus (cc) and posterior to posterior semicircular canal (psc). Canal of subarcuate artery (csa) lies inferior to superior semicircular canal (ssc).

See key for abbreviations.

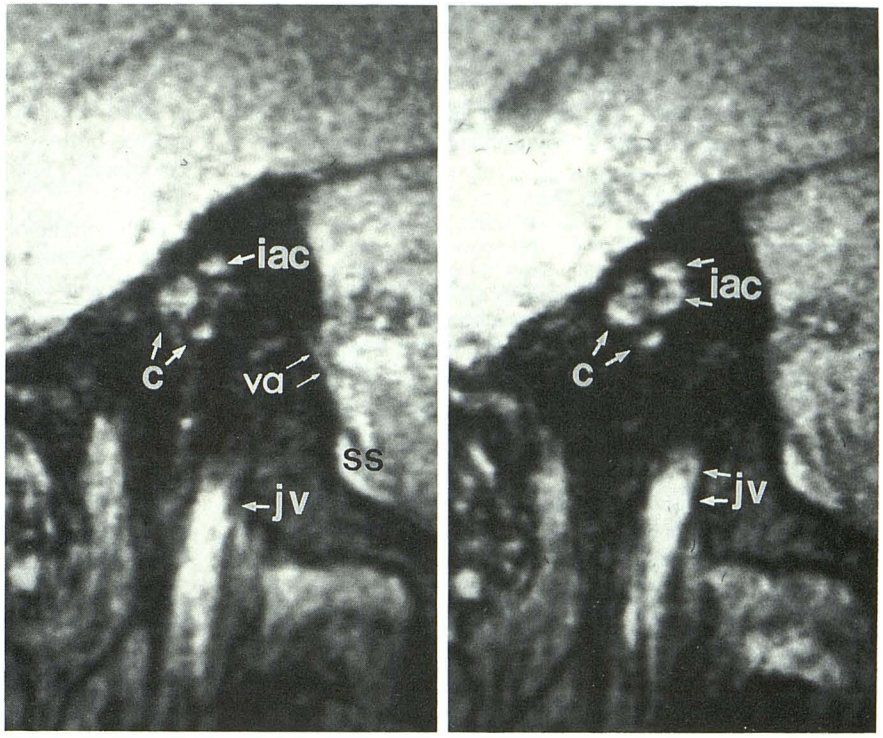

Fig. 15.—Sagittal 3DFT MR images. See key for abbreviations.

***A*, At level of fundus of internal auditory canal. Medial extent of vestibular aqueduct (va) is seen.**

***B*, 1.0 mm mediad. Fundus of internal auditory canal (iac) lies posterior to cochlea (c) and appears segmented.**

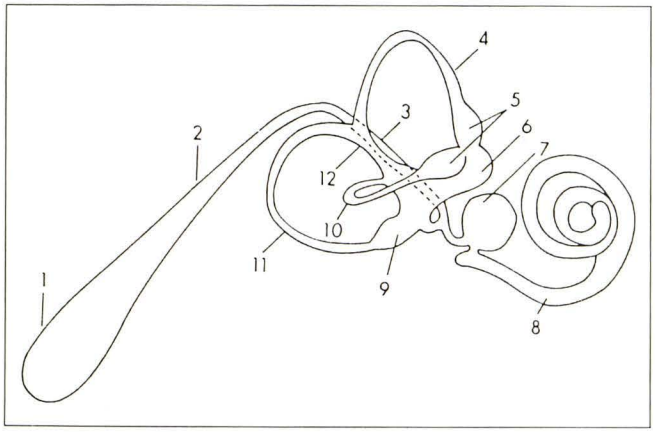

Fig. 16.—Schematic lateral view, right membranous labyrinth. 1 = endolymphatic sac, 2 = posterior limb of endolymphatic duct, 3 = short anterior limb of endolymphatic duct, 4 = superior semicircular canal, 5 and 9 = ampullae, 6 = utricle, 7 = saccule, 8 = cochlear duct, 10 = lateral semicircular canal, 12 = common crus. Note short anterior limb of endolymphatic duct (3) mediad to and superimposed on common crus (12). (Reprinted with permission from Rumbaugh et al. [20].)

coil and 12-cm FOV. The small surface coil provides inherently higher signal to noise than the standard head coil. With the small FOV and the surface coil, we found that wraparound artifact was not a serious problem because little signal was generated from the deep cerebral structures.

The 30° axial and 120° coronal 1.5-mm-thick high-resolution CT bone-algorithm images were obtained on a Technicare 1440 scanner with a 512 × 512 matrix, 130 kV, 400 mAs, and 20-cm scan diameter. The sagittal images were obtained on a Technicare 2060 CT scanner with a 512 × 512 matrix, 120 kV, 600 mAs, and 13-cm scan diameter.

Results

The fluid-filled structures of the otic capsule were seen on the 3DFT images as high-signal foci surrounded by the signal void of air and bone. These structures include the flared cochlear aqueduct (Fig. 1); the small linear tensor tympani muscle projecting into the signal void of the middle ear cavity (Fig. 2); the perilymph and endolymph within the curvilinear semicircular canals, which appear punctate on cross section and crescent-shaped in the image plane (Fig. 4A); the ovoid vestibule (Fig. 4A); the hockey-stick–shaped vestibular aqueduct (Fig. 4A); the entire facial nerve, including the geniculate ganglion (Fig. 4A); and the coiled cochlea (Fig. 7). The chorda tympani nerve was not visualized. Although the lumen of the external ear canal is a signal void, the periosteum lining the canal floor appears as a thin, linear high-signal region (Fig. 7). The carotid artery and jugular vein demonstrated high signal secondary to flowing blood (Figs. 1 and 15).

On axial and coronal MR images (Figs. 4A and 9), the internal auditory canal demonstrates predominantly high signal intensity, reflecting the presence of CSF within the lumen [6]. An interesting observation is the regional variation of CSF signal intensity within the internal auditory canal. The signal intensity in the fundus is higher than in the more mediad portions of the lumen and CPA. This suggests that the fluid within the fundus, like that in the vestibule and cochlea, is relatively static in comparison with the more pulsatile CSF in the CPA cistern and porus acusticus (Fig. 5).

The volume averaging inherent in the high-resolution thin-section CT technique, used in conjunction with a bone algorithm, minimizes visualization of the small soft-tissue components of the otic capsule and middle ear. The osseous and

aerated temporal bone structures that are well seen on high-resolution CT include the dense bone of the otic capsule, small crescent-shaped lucencies of the semicircular canals, the facial nerve canal, the vestibular aqueduct, the coiled lucency of the cochlea, and the oval and round windows (Figs. 4B and 14C).

Discussion

High-resolution imaging of the bony architecture of the inner ear is best achieved by high-resolution CT. With a bone algorithm, high-resolution CT provides detail of small osseous structures. The high level of resolution allows early diagnosis of disease entities such as otosclerosis, mastoid opacification, trauma, cholesteatoma, and congenital anomalies [3]. Intrathecal injection of subarachnoid air or a water-soluble contrast agent is required to delineate subtle abnormalities in the CPA and internal auditory canal [16, 17]. MR has proved highly valuable in demonstrating early disease changes in the CPA, including seventh or eighth cranial nerve schwannoma, tortuous CPA vascular loop, meningioma, Bell palsy, and carcinomatosis [4, 5]. The spatial resolution of standard 2DFT spin-echo MR techniques has been limited by a slice thickness greater than 3 mm. This thickness is less than ideal for some otic capsule disorders, in which early disease changes may be submillimeter in size.

Our new 3DFT MR imaging technique provides high spatial resolution and signal to noise, which increases visualization of the soft-tissue structures of the inner ear. Very small structures, such as the endolymphatic duct and sac, are demonstrated routinely. This improved resolution may allow demonstration of abnormalities such as a CSF fistula and evaluation of vestibular duct shunt function, microtrauma, labyrinthine tumors, vestibulitis, Bell palsy, Meniere disease, congenital anomalies, and intralabyrinthine hemorrhage. This technique also may generate new insights into other entities, such as otosclerosis, which are generally described in terms of osseous changes.

On gradient-refocused echo images, factors that contribute to focal field inhomogeneities lead to spin dephasing and secondary signal loss [15]. These factors include focal differences in magnetic susceptibilities. The magnetic susceptibility differences, especially between soft tissue, bone, and air, lead to local variations in the magnetic field strength. Shortening the TE minimizes the spin dephasing secondary to magnetic susceptibility homogeneities. Our technique uses very short TEs (7 msec) to minimize magnetic susceptibility effects [12].

The high signal intensity in the fundus of the internal auditory canal is probably related to the steady-state conditions of the GRASS technique. The pulsatile CSF in the CPA may decrease the spin coherence and disrupt the steady-state conditions, possibly accounting for the low signal intensity seen within the CPA (Figs. 4A and 9). CPA CSF flow artifacts are commonly seen on routine spin-echo images.

Spatial resolution improves with thinner slice thickness as long as there is adequate signal to noise. When imaging the microstructures of the otic capsule, adequate spatial resolution requires millimeter- or submillimeter-thick slices (0.5–1.0 mm). Slice thicknesses available with previous standard 2DFT MR techniques are limited to approximately 3.0 mm, with severe degradation of signal to noise and image quality with thinner slices.

Although the standard head coil provided adequate signal to noise for evaluation of the CPA, use of a 3-in. surface coil allowed better centering of the otic capsule structures within the smaller FOV and yielded significantly improved signal to noise.

High correlation was found between the otic capsule structures delineated on high-resolution CT and 3DFT MR images. The CT and standard MR appearance of otic capsule structures is well established [1]. However, several small soft-tissue structures such as the endolymphatic duct and sac were uniquely delineated by the 3DFT technique, while important membranous structures such as the oval and round windows were better seen on high-resolution CT. Other structures such as the tensor tympani muscle, carotid artery, jugular vein, and subarcuate artery were visualized by both techniques, but the soft-tissue components were better characterized on the 3DFT MR images.

The vestibular aqueduct is a tiny bony canal that courses posterolaterally through the posterior aspect of the petrous bone, parallel to the posterior semicircular canal. The aqueduct measures 3.5–12.0 mm in length, with an average diameter of 0.17 mm [18–20]. Distally, the aqueduct ends near the sigmoid sinus at the external aperture, a small (<8.0 mm) ovoid opening that lies below an overhanging ridge of bone, the operculum. On high-resolution CT, the aqueduct appears as a thin, linear lucent defect coursing inferiorly from the common crus through the posterior petrous bone (Fig. 14C).

The vestibular aqueduct contains the endolymphatic duct and sac, minor components of the membranous labyrinth that are filled with endolymph (Fig. 16). The duct is an endothelium-lined tube that arises from the confluence of the saccular and utricular ducts within the vestibule, bathed in perilymph. The middle segment, or isthmus, of the endolymphatic duct lies within the vestibular aqueduct and courses mediad to the common crus. The isthmus measures approximately 1.6 mm in length and 0.05 mm in diameter. In the distal segment of the aqueduct, the endolymphatic duct broadens and flattens to form the endolymphatic sac. The endolymph within the endolymphatic duct and sac appears as a thin, high-intensity linear focus on MR. Within the vestibule, the saccule, utricle, and proximal segment of the endolymphatic duct are indistinguishable from the surrounding perilymph (Fig. 4). On axial (Figs. 3–5) and sagittal (Figs. 12, 13, 14A, and 14B) MR images, the endolymphatic duct is seen coursing inferiorly and posterolaterally from the region of the common crus toward the posterior cranial fossa. On axial (Fig. 3) and sagittal (Figs. 14A and 14B) MR images, the endolymphatic sac appears as increased signal within the external aperture, underlying the operculum, and separated from the subarachnoid space of the posterior fossa by the dura (which appears as a thin, hypointense, linear focus).

The oval and round windows are best seen on high-resolution CT and can be identified in all three planes. On axial (Fig. 3) and coronal (Fig. 9) MR images, the oval window can be approximated by location of adjacent structures such as the vestibular cecum of the basal turn of the cochlea, the vestibule, and the tympanic portion of the facial nerve coursing

inferior to the horizontal semicircular canal. The round window is not directly identified on axial or sagittal MR but, in the coronal plane, can be approximated by adjacent structures such as the vestibule and the tympanic portion of the facial nerve.

In the anterior aspect of the middle ear cavity, the tendon of the tensor tympani muscle emerges from the semicanal of the tensor tympani muscle. The tendon of the tensor tympani muscle hooks around the cochleariformis process as it courses through the middle ear cavity to insert onto the manubrium of the malleus. On MR (Fig. 2), the tensor tympani muscle appears as a thin, linear, high-signal region parallel to the carotid artery. Because of low proton density, the tendon is not visualized on MR.

Several of the major vessels of the skull base are included on the images, including the petrous portion of the internal carotid artery, the jugular vein, and the sigmoid sinus. Axial MR (Fig. 1) demonstrates flow-related high signal intensity delineating the lumen of the petrous portion of the carotid artery [11]. The jugular vein is visualized on sagittal MR (Fig. 15) as a linear high-signal focus coursing superiorly into the floor of the petrous bone, ending at the level of the sigmoid sinus [13].

In the superior aspect of the otic capsule, the canal of the subarcuate artery is seen coursing laterally from the posterior aspect of the petrous apex, toward the superior semicircular canal. This tiny bony canal represents the remnant of the major fetal blood supply to the developing otic capsule structures. On axial MR (Fig. 6), the soft-tissue contents of the canal appear as a smoothly angled, high-signal, thin, linear focus that courses deep into the otic capsule, between the anterior and posterior limbs of the superior semicircular canal. This relationship is demonstrated on coronal (Fig. 10) and sagittal (Fig. 13) projections.

REFERENCES

1. Brogan MB, Chakeres DW. Computed tomography and magnetic resonance imaging of the normal anatomy of the temporal bone. *Semin Ultrasound CT MR* **1989**;10:178–194
2. Enzmann DR, O'Donohue J. Optimizing MR imaging for detecting small tumors in the cerebellopontine angle and internal auditory canal. *AJNR* **1987**;8:99–106
3. Mafee M, Kumar A, Tahmoressi C, et al. Direct sagittal CT in the evaluation of temporal bone disease. *AJNR* **1988**;9:371–378, *AJR* **1988**;150:1403–1410
4. Press GA, Hesselink JR. MR imaging of cerebellopontine angle and internal auditory canal lesions at 1.5 T. *AJNR* **1988**;9:241–251
5. Daniels DL, Millen SJ, Meyer GA, et al. MR detection of tumor in the internal auditory canal. *AJNR* **1987**;8:249–252
6. Valvassori GE, Morales FG, Palacios E, Dobben GE. MR of the normal and abnormal internal auditory canal. *AJNR* **1988**;9:115–119
7. Chakeres DW, Spiegel PK. A systematic method for comprehensive evaluation of the temporal bone by computed tomography. *Radiology* **1983**;146:97–106
8. Chakeres DW. Clinical significance of partial volume averaging of the temporal bone. *AJNR* **1984**;5:297–302
9. Brogan M, Chakeres DW. Gd-DTPA–enhanced MR imaging of cochlear schwannoma. *AJNR* **1990**;11:407–408
10. Harms SE, Flamig DP, Fisher CF, Fulmer JM. New method for fast MR imaging of the knee. *Radiology* **1989**;173:743–750
11. Hale JD, Valk PE, Watts JC, et al. MR imaging of blood vessels using three-dimensional reconstruction: methodology. *Radiology* **1985**;157:727–733
12. Schmalbrock P, Yuan C, Chakeres DW. Volume MR angiography: methods to achieve very short TE. *Radiology* **1990**;175:861–865
13. Masaryk TJ, Modic MT, Ross JS, et al. Intracranial circulation: preliminary clinical results with 3-D (volume) MRA. *Radiology* **1989**;171:793–799
14. Ludeke KM, Roschmann P, Tischler R. Susceptibility artifacts in NMR imaging. *Magn Reson Imaging* **1985**;3:329–343
15. Shaw D. Fundamental principles of nuclear magnetic resonance. In: Wherli F, Shaw D, Kneeland JB, eds. *Biomedical magnetic resonance imaging: principles, methodology, and applications*. New York: VCH, **1988**:1–46
16. Pinto RS, Kricheff II, Bergeron R, Cohen N. Small acoustic neuromas: detection by high-resolution gas CT cisternography. *AJNR* **1982**;3:283–286
17. Steele J, Hoffman J. Brainstem evaluation with CT cisternography. *AJNR* **1980**;1:521–526
18. Anson BJ, Donaldson JA. *Surgical anatomy of the temporal bone*, 3rd ed. Philadelphia: Saunders, **1981**:166–178, 228–231, 300–320, 480–495, 590–615
19. Ballinger J. *Diseases of the nose, throat, and ear*. Philadelphia: Lea & Febiger, **1977**:605–651
20. Rumbaugh CL, Bergeron T, Scanlan RL. Vestibular aqueduct in Meniere's disease. *Radiol Clin North Am* **1974**;12:517–525

The reader's attention is directed to the commentary on this article, which appears on pages 17–18.